X-ray propagation-base phase-enhanced imaging of the meniscus of a capillary flow in a rectangular microchannel

Alexandre Vabre, Samuel Legoupil, Stéphane Colin, Sandrine Geoffroy, Wah-Keat Lee, Kamel Fezzaa

X-RAY PROPAGATION-BASE PHASE-ENHANCED IMAGING OF THE MENISCUS OF A CAPILLARY FLOW IN A RECTANGULAR MICROCHANNEL

Alexandre Vabre*, Samuel Legoupil*, Stéphane Colin°, Sandrine Geoffroy°, Wah-Keat Lee*, Kamel Fezzaa*

*CEA LIST, 91191 Gif sur Yvette, France, °INSA, 31077 Toulouse cedex 4, France, *APS, Argonne, Illinois 60439, USA

ABSTRACT

We present in this paper a three-dimensional technique for analysing the meniscus of a capillary flow in a rectangular microchannel. Due to strong experimental constraints, both on the high flow dynamics and on the small dimensions of the channel, we use a synchrotron beam provided by the Advanced Photon Source of Chicago, which presents numerous advantages. First, the beam has a high spatial coherence, and it is then possible to perform x-ray phase contrast imaging. This technique exploits refractive index variations and is 100 to 1000 times more sensitive than classical absorption techniques. Second, emission fluxes of x-ray photons are very important, and rapid dynamics measurements are possible. This unique imaging technique allows carrying out measurements on samples of very low dimensions (a few tens of micrometers), produces 3D images and can be implemented on substrates opaque to visible light. The tested microchannel section is 25 µm deep and 100 µm wide. The substrate is PDMS exposed to oxygen plasma beforehand to be hydrophilic and the fluid is pure water. Measurements are made at different projection angles comprised between -75° and +75°, in order to apply tomography techniques. A 3D image of the meniscus is then reconstructed.

1. INTRODUCTION

Developing experimental techniques for accurate analysis of two-phase flows in microchannels is a current challenge. Applications dealing with such microchannel flows are very large and concern biology or process engineering for which integration of microchannels in lab-on-chip or micro-reactors is a strong stake. Our work is focused on developing a measurement technique to characterize the three-dimensional meniscus of a flow in a rectangular microchannel.

The accurate knowledge of local contact angles between the fluid and walls is fundamental, especially to implement a smart modelling approach of the imbibition phase. Experimental constraints are high: spatial scales are in the order of 10 µm, implying very low contrasts. Also, flow dynamics is relatively rapid (in the order of a few cm/s) and implies a high acquisition frequency, around 100 Hz. For these two reasons, we use a synchrotron beam provided by the Advanced Photon Source of Chicago, which presents numerous advantages. This unique imaging technique allows carrying out measurements on samples of very low dimensions (less than 100 µm) and produces 3D images. The tested microchannel is 100 µm wide, 25 µm deep and the substrate is PDMS. The fluid is pure water and is injected by the bottom of the channel, which is placed vertically.

In what follows, we present our preliminary efforts and results toward this objective using the phase-enhanced imaging technique.

The paper is indented in four main parts, as follows. First, the phase contrast method is presented in detail. Second, the experimental set-up is described and the acquired images of flows in the microchannel are presented. Third, the method for tomographic reconstructions is presented and meniscus 3-D profiles are built and analyzed. Finally, we conclude the paper with a discussion and a presentation of perspectives for this work.

2. PHASE CONTRAST METHOD

Away from the Bragg diffraction condition, the transmission of x-rays through a material can be described by the material's complex index of refraction, *n*, which is usually written as:

$$n = 1 - \delta + i\beta \quad (1)$$

As in visible light optics, the x-ray wave vector in the material is modified by the index of refraction such that the x-ray wave vector inside the material $k' = n\,k$, where $k = 2\pi/\lambda$ is the vacuum wave vector, and λ is the wavelength of the x-ray. The linear absorption coefficient μ is related to the imaginary part of the index of refraction:

$$\mu = \frac{4\pi\beta}{\lambda}. \qquad (2)$$

For most applications, the dominant contribution to the absorption is the photoelectric effect. In this case, the linear absorption coefficient varies approximately [1] as

$$\mu_{p.e.} \sim \rho\,\lambda^3\,Z^4 \qquad (3)$$

where ρ is the density of the material and Z is the atomic number. In the x-ray regime, and away from absorption edges and Bragg conditions, it can be considered with a good approximation that

$$\delta \approx 1.3\times10^{-6}\,\rho\,\lambda^2. \qquad (4)$$

δ is thus a small positive number of the order of 10^{-6}. The x-ray phase velocity, c/n, is therefore higher inside the material than in vacuum.

For an incident plane wave of unit amplitude travelling in the *z*-direction,

$$\Psi_0 = e^{ikz} \qquad (5)$$

the transmitted wave immediately after the sample can be written as

$$\Psi_1 = A(x,y)\, e^{i\varphi(x,y)}\, e^{ikz} \qquad (6)$$

where

$$A(x,y) = e^{-\frac{\int \mu(x,y,z)\,dz}{2}} \qquad (7)$$

and

$$\varphi(x,y) = -\frac{2\pi}{\lambda}\int \delta(x,y,z)\,dz\,. \qquad (8)$$

In conventional absorption x-ray imaging, the detector is usually placed close to the sample. The measured intensity is thus:

$$I^{abs}(x,y) = \left|\Psi_1\right|^2 = e^{-\int \mu(x,y,z)\,dz} \qquad (9)$$

where the integration is over the sample. The intensity at each point on the detected image (radiograph) depends on the integrated absorption suffered by the corresponding x-ray beam through the sample. Thus, a radiograph provides information regarding the sample absorption coefficient projected onto the *x*-*y* plane, $\mu(x,y)$. By using tomographic techniques, it is possible to obtain $\mu(x,y,z)$. The contrast mechanism can be fully described by a geometrical-ray approach. The intensity at each point on the detector only depends on how much energy the particular ray loses as it traverses the sample. Neighbouring rays have no effect (aside from blurring due to instrumental resolution and finite source size). The contrast mechanism has nothing to do with diffraction or interference.

In phase-enhanced x-ray imaging, the contrast mechanism is based on diffraction and/or interference that results from the differences in the real part of the index of refraction within the sample. Note that this is in addition to the normal absorption contrast mechanism. There are three techniques that can provide phase-enhanced images in the x-ray regime: (1) interferometry [2; 3], (2) angular deflectometry [4; 5] and (3) Fresnel diffraction via propagation [6; 7].

In the technique described in this paper, propagation-based Fresnel diffraction, the contrast mechanism comes from the interference between neighbouring points of the wavefront at a certain distance from the sample. The advantages of this technique are: (1) very high flux since minimal x-ray optics are required, (2) simplicity as a result of its in-line geometry, and (3) almost any sample size can be used.

Fresnel diffraction can be described by the Fresnel-Kirchoff integral [8]. The wave excitation at a point *P* on the detector at s_0 away from the sample can be written as:

$$\Psi_P(x,y) = \frac{-i\, e^{iks_0}}{\lambda\, s_0}\iint \Psi_1(x',y')\, e^{ik\left(\frac{(x-x')^2+(y-y')^2}{2s_0}\right)}\, dx'\, dy' \qquad (10)$$

where the integration is over the plane of the sample. This equation describes the propagation of the wave from the sample to some distance away, and it is this propagation that allows for the interference effect responsible for this imaging technique. From equation (10), clearly the wave functions at each and every point on the sample plane contribute to the wave function at each and every point of the detector plane. However, since the exponential in the integral fluctuates rapidly for large ($x - x'$) and ($y - y'$), most of the contributions to the wave function at (x_i , y_i) come from a region near the corresponding point on the sample. The choice of the sample to detector distance, s_0, depends on the sample characteristics, the x-ray wavelength, and the desired features to be detected. Generally, the smaller the x-ray wavelength, the larger is the required distance for the interference to occur. The distance also acts as a Fourier filter in that images taken at smaller distances will be more sensitive to higher sample spatial frequencies while images taken at larger distances will be more sensitive to lower sample spatial frequencies.

Several aspects of this technique should be pointed out. Since this technique involves interference between transversely nearby points of the wavefront, the incoming wave must be at least partially spatially coherent. The small source size and large source-to-sample distances at third-generation synchrotrons like the Advanced Photon Source (APS) provide x-ray beams that easily satisfy the spatial coherence requirement. Another important consideration is the required beam monochromaticity. Although the index of refraction and the Fresnel-Kirchoff integral depend on the x-ray wavelength, it can be shown [9] that, for the edge-enhanced regime that is of interest here, the dependence is weak. That is to say, although the exact interference fringe structure is wavelength dependent, the largest peak/valley features near the phase jumps are not very sensitive to the wavelength. Thus, if, as in this case, one is only interested in seeing the edges of the sample, a broad energy bandpass incident beam can be used. In fact, this technique has been demonstrated using a synchrotron white beam [10].

3. EXPERIMENTAL SET-UP AND ACQUIRED IMAGES

3.1 Experimental set-up

The experiments were performed at the SRI-CAT 1-ID-C station at the APS. A high-energy bent Laue silicon monochromator [11] provided a monochromatic beam to the sample with an energy bandpass $\Delta E/E \sim 10^{-3}$. The employed energy during experiments was 25 keV. The x-ray beam size was approximately 1 mm^2, and the total number of incident photons on the sample was about 10^{11} ph/s. The source-to-sample distance was about 60 m, and the sample-to-detector distance was about 50 cm. A 400 µm thick $CdWO_4$ crystal was used to convert x-rays to visible light. The image was magnified using a microscope lens (x5) and recorded with a cryogenically cooled CCD (1024x1280 pixels, 6.7 µm pixel size) detector. So pixel size in the sample is 1.34 µm and the field of view in the plate is 1.37x1.72 mm^2.

The microchannel plate is disposed in a metallic frame in order to keep it flat. The plate is made of 13 microchannels. All the channels are 25 µm deep (along z-axis) and 45 mm long (along x-axis), only the width changes between 10 and 500 µm (along y-axis). The results presented in this paper are relative to a 100 µm wide microchannel. The chosen fluid is pure water. It is injected in the microchannel through a syringe and a tube from outside of the shielded room. Fluid is injected by the bottom reservoir and the flow is going up through capillary pumping. After an injection, air is blown into the microchannel to dry it and to be ready for another injection.

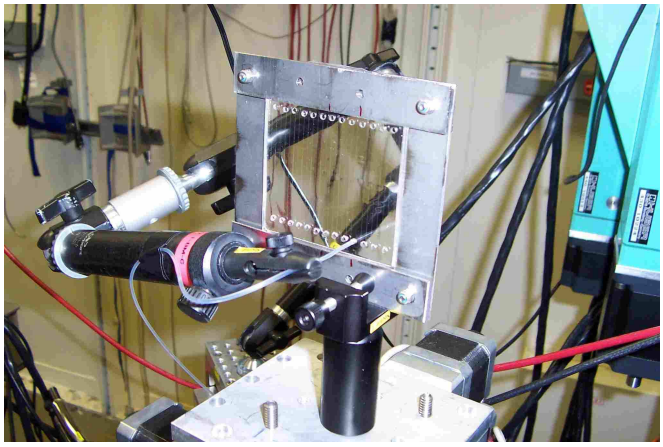

Figure 1: Photograph of the set-up

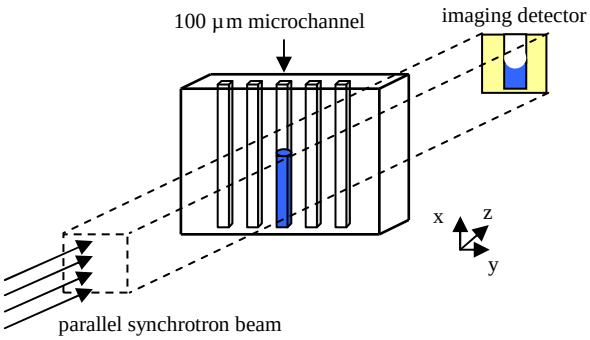

Figure 2: Diagram of the set-up

A photograph of the microchannel plate is shown in figure 1. We can see the arm that positions the tube for an injection of water in the bottom of microchannel. Figure 2 is a diagram of the experiment.

3.2 Acquired images

A limitation here is that PDMS substrate containing the channels presents a high aspect ratio (width over thickness). The dimensions of the substrate are 45x50x4 mm^3. Then 31 projections has been acquired for angles equally distributed in the range [-75°; +75°] around the *x*-axis (figure 3), covering a global angle of 150°. Acquisition of projections at higher angle was not possible due to the 1/cos(angle) relation of the material thickness seen by the x-ray beam. At higher angles, the absorption of material becomes too high and images are too much noisy or even inexistent to be processed.

For each projection that follows, an injection of water has been carried out. A hypothesis of repeatability of the flow conditions has been made; indeed, it was not possible to realize all the projections for the same injection due the quite high flow velocity and rotations of the sample take time. We performed an injection for each acquisition. So images had to be realigned to always get the meniscus in the same position in the image to make post-processing possible. Also, gains have been normalized in the images to take into account variations in time of the detector.

The flow velocity is in the magnitude of 5 cm/s, which is quite high as compared to the limited field of view. The exposure time had to be very short (5 ms), in order not to introduce blur in the image. Another possibility would be to trig optically acquisitions with another signal, optical for example.

In conventional x-ray computed tomography, 180° or 360° projection angles are required with specific conditions between the detector resolution and the number of projections. So 30° angle scan is missing to fulfil the latter requirement. This introduces a bias in the coming tomographic reconstructions.

Here follow three images of 2D images of meniscus (figure 3).

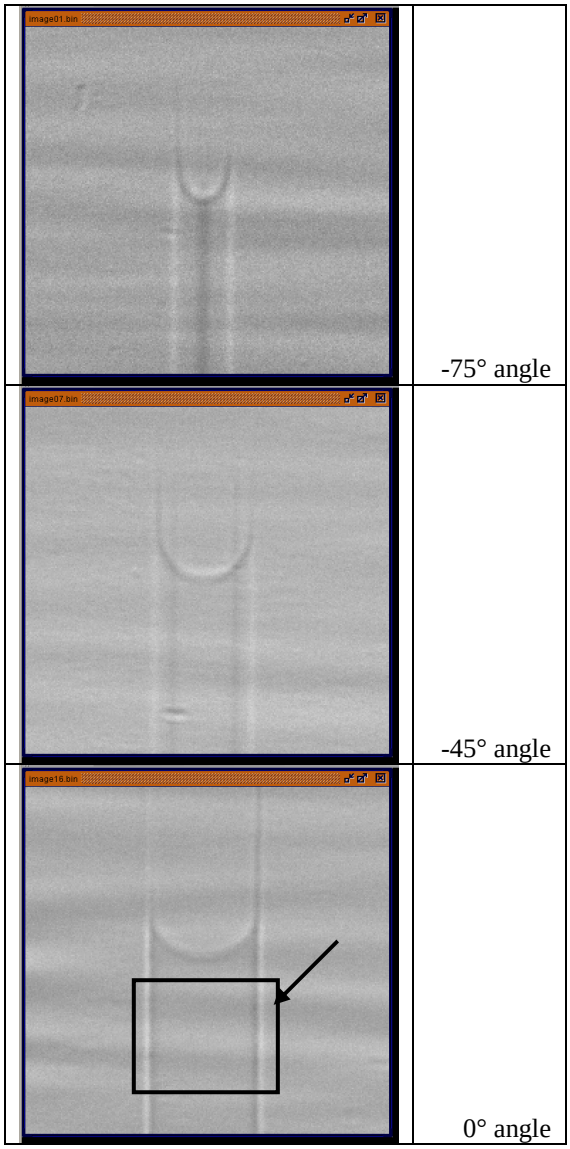

Figure 3: 2D images of the flow

The corresponding profiles are plotted in figure 4. Each profile is an integration of the image value in the area shown in figure 3.

These profiles are characteristic of phase contrast effect with oscillations at the location of edges and an almost constant value outside from edges. This is the information provided by phase contrast measurements: a peak at the location of edges. This data is then analysed as density gradient information in the image. The same level is observed in the PDMS substrate and in the channel filled or not with water. This is due to a very low contrast of absorption between the three media, and it implies that conventional absorption x-ray could not have been applied.

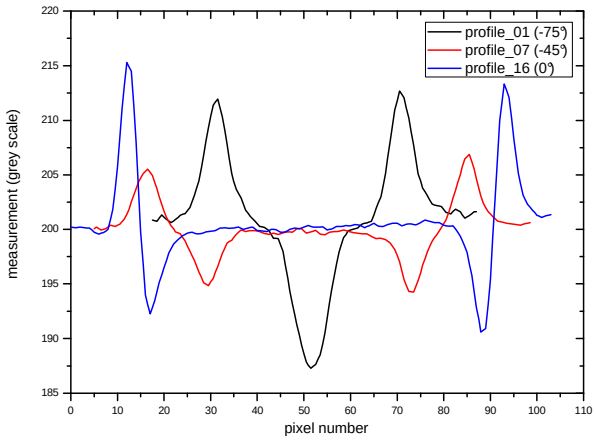

Figure 4: profiles in images for different projection angles

4. TOMOGRAPHIC RECONSTRUCTIONS

Images acquired with the set-up were converted into sinograms. Normalization procedures were applied in order to equalize gain detector and beam light inhomogeneity in the images. The sinograms are obtained by applying a procedure which rearranges the data in a specific way. A sinogram collects the lines in the images presented in figure 3 at a given *x*-position along the axis of rotation, *i.e.* the axis of the channel, as a function of angles. As such, a sinogram consists of 31 lines per 106 rows, each row corresponding to a pixel in the region of interest which includes the meniscus. An example of sinogram is shown in figure 5.

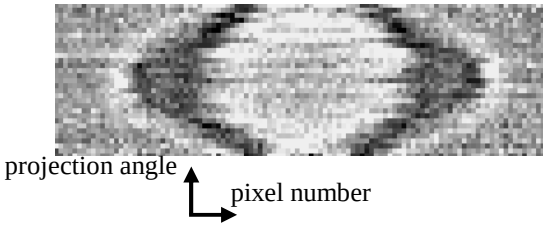

Figure 5: example of sinogram

The width of the region of interest is 106 pixels, which corresponds to the width of the channel. Despite the high flux of photons in the beam, the exposure time is very low (5 ms) and the images are quite noisy. The distributions have been reconstructed by integrating the filtered projections on 150° instead of 180°. Back projection has been realized on only 150°.

In conventional x-ray tomography, it is assumed that the projection data are the Radon transform of the function to be estimated. Noting δ' the Dirac function, the two-dimensional Radon transform expressed as

$$R[f(s,w)] = \iint_{\Re^2} f(x,y)\delta'(s - x\sin w - y\cos w)dx\,dy \quad (11)$$

describes the integration of function *f*(*x*, *y*) over the lines defined by the scalar *s*, in the detector coordinate system and the angle *w* which is the projection angle of the sample in the beam. As the set-up makes use of parallel x-ray beam, the three-dimensional distribution of the refractive index is reconstructed as a stack of two-dimensional distributions. Each of these distributions is reconstructed by applying the filtered back projection (FBP) algorithm, making the hypothesis that the contribution of the wave excitation at a point on the detector comes from a close region of it. It means that no deconvolution procedure of the interference effect is applied on the images. As a consequence, this approximation makes the spatial resolution weak and could be enhanced by applying proper algorithm [12]. We also consider that the $A(x, y)$ function is constant and the measurement is only a function of $\varphi(x, y)$, which integrates for a given z the refractive index distribution $\delta(x, y, z)$ (*cf.* equations (6) and (7)).

The filtered back projection algorithm allows to recover the $f(x, y)$ distribution by considering the projection data at angles in the range $[0,\pi[$:

$$f(x,y) = \int_0^{\pi} p'(s,w)dw \quad (12)$$

with $p'(s,w) = \int_{-\infty}^{+\infty} \tilde{p}(\rho,w)|\rho|W(\rho)e^{i2\pi\rho u}d\rho$ where $\tilde{p}(\rho,w)$ is the Fourier transform of $p(s, w)$. $W(\rho)$ is an apodization filter which limits the noise effect at high frequency enhanced by the ramp filter $|\rho|$. Many filters can be applied. Best results have been obtained with 9th order Butterworth filter with a cut-off frequency equal to 0.3 of the Nyquist frequency. The FBP algorithm simply tells that the $f(x, y)$ function is obtained by backprojecting the projections filtered with a ramp and an apodization filters.

The FBP algorithm was applied for the 256 sinograms generated along the vertical direction of the detector. Then 256 cross-sections images of the microchannel were obtained. It was possible to pile up and interpolate these images to constitute a 3D image. This image of the shape of the meniscus is shown in figure 6. The full time to reconstruct such an image is around 1 hour.

We can observe on the reconstructed images that the surface described by the meniscus is really 3D. A curvature appears in the transversal direction that provides a lot of information. This is the main gain of this measurement technique as compared to optical ones; we can plot the 3D surface that describes the meniscus. At this stage, due to the algorithm we applied, the information is qualitative.

PDMS is naturally a hydrophobic substrate, but the bonding process requires a surface treatment with oxygen plasma. After exposition to oxygen plasma, PDMS surface becomes hydrophilic [13], and the shape of the first observed interfaces (figure 6) is in accordance with the expected profile.

The further objective will be to confront these experimental data to theoretical knowledge for a better understanding of capillary flows behaviour in rectangular microchannels. Basic understanding of the capillarity laws was gained almost a century ago [14; 15; 16; 17; 18]. Since then, the Lucas-Washburn equation has been serving for decades as the basis for describing the capillary phenomena [19; 20; 21].

However, there are critical hydraulic diameters and flow rates, above which dynamic inertia effects can no longer be neglected [22; 23; 24]. The Washburn equation has also been shown to be insufficient at very short times partly due to the lack of inertial terms [17].

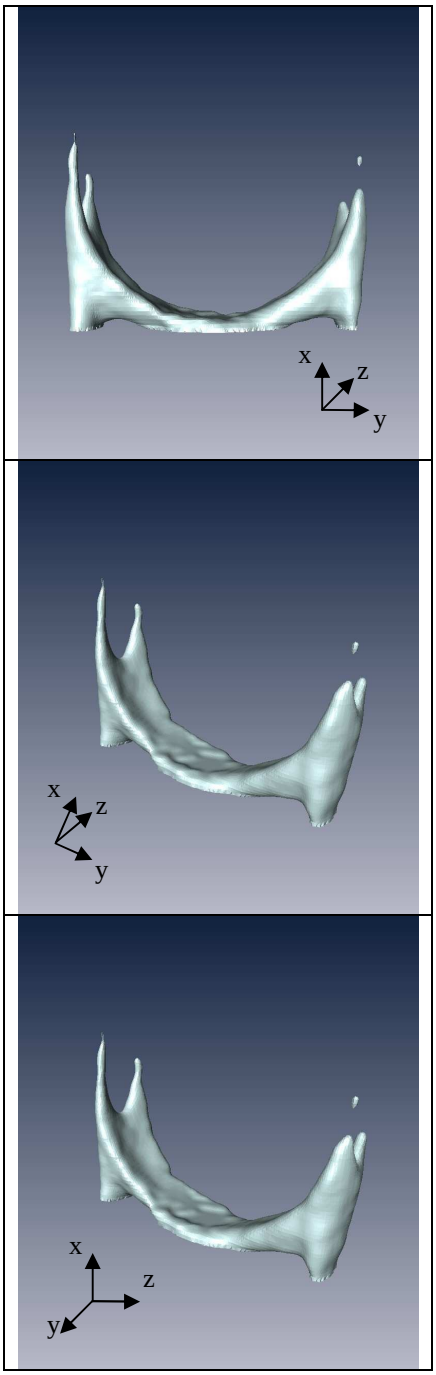

The x-ray technique described in this article will enable to review the mechanisms controlling the dynamics of capillary rise and determine the main forces acting on the liquid (balance of dynamic inertia, surface tension, gravity and viscosity of the liquid). Surface tension is dependant on contact angle and by studying meniscus shape, the x-ray technique will confirm or not the flow rate-dependent dynamic contact angle found by Hamraoui *et al*. [25]

More widely, this technique will enable to study:

- the initial stages of penetration (for which inertia effects are significant [22; 23]),
- surfactants effects [26],
- the effects of preparation and cleaning of capillaries, which are essential for the liquid-substrate interaction.

5. DISCUSSION

The x-ray images shown in figure 3 were taken with an incoming beam of energy 25 keV, with a bandpass $\Delta E/E \sim 10^{-3}$, and a 5 ms exposure time. Furthermore, the undulator x-ray source was specifically detuned to about 1/30th of its maximum intensity at this energy to prevent saturation of the detector. The photon flux onto the sample over the beam area ($\sim 1 \times 1$ mm^2) was about 10^{11} ph/s.

As described above, it is not necessary for the incoming beam to have a narrow bandpass. By using a multilayer monochromator or a multilayer mirror [27] instead of single-crystal silicon, the energy bandwidth of the incoming beam can be increased to $\Delta E/E \sim 10^{-2} - 10^{-1}$. This would boost the incoming photon flux by a factor of about 10-100. Taken together with another generation of detector, photon counting detector to eliminate noise, images presented in figure 3 can be much noiseless.

It can be seen that phase-enhanced radiography at 5 ms time resolution can be achieved but even much better exposure time is possible on such facility. The fast time resolution afforded by this technique has allowed us to clearly visualize flows in microchannels. The unique ability of this x-ray imaging technique should prove to be useful in validating computational fluid dynamics results obtained from microchannels.

At a first step, the standard filtered back projection algorithm has been used with strong hypothesis which are not satisfied here. The effect of interference waves on the detector could be taken into account by a pre deconvolution algorithm or by considering it directly in the reconstruction procedure. Besides, the lack of projections in a certain angle range and the small number of projections could be taken into account by applying discrete methods for reconstruction rather than analytical one which requires 180° projections. The resolution should be deeply enhanced in that case and measurements could become quantitative. This gives perspective to that work.

6. CONCLUSION

The simplicity of the propagation-based phase-enhanced imaging technique described here, together with the availability of the very high flux and high x-ray energies opens up many exciting possibilities in the field of x-ray imaging. In the current experiments involving microchannels, radiography in the 5 ms range can be achieved.

This preliminary work has allowed representing the 3D shape of a meniscus in a capillary flow. The main difficulties of this work were the high dynamics of the flow. As a consequence, images had to be acquired during very short times. The results are very encouraging; it has been possible to perform acquisitions on a very powerful instrument such as a synchrotron. Another difficulty was tomographic reconstructions of the data. Indeed, we had a partial data set of 150° projections of the microchannel. Also, algorithms for that kind of reconstruction are quite different from the ones for absorption computed tomography. Despite these difficulties, very interesting images were obtained. It is clear on these images that the meniscus surface is purely 3D and presents a transversal curvature that can not be observed using optical techniques.

Perspectives of this work are to compare the experimental 3D image of the meniscus with a CFD

simulation result. This comparison will improve a lot the knowledge and hypothesis made on such capillary flows. Also, another perspective is to obtain other meniscus images for different types of substrate and surface treatments and to study more complex configurations such as those encountered in bifurcations. This will allow disposing of data base on capillary flows in microchannels.

7. ACKNOWLEDGEMENTS

Use of the Advanced Photon Source was supported by the U.S. Department of Energy, Office of Science, Office of Basic Energy Sciences, under Contract No. W-31-109-ENG-38. Microchannels were provided by the LAAS-CNRS, Toulouse.

8. REFERENCES AND CITATIONS

1. Als-Nielsen, J., and McMorrow, D., 2001, *Elements of Modern x-ray Physics*, John Wiley and Sons, New York.
2. Beckmann, F., Bonse, U., and Biermann, T., 1999, New developments in attenuation and phase-contrast microtomography using synchrotron radiation with low and high photon energies, *Developments in X-Ray Tomography II*, SPIE **3772**, 179-187.
3. Momose, A., Takeda, T., Itai, Y., Tu, J., and Hirano, K., 1999, Recent observations inphase-contrast x-ray computed tomography, *Developments in X-Ray Tomography II*, SPIE **3772**, 188-195.
4. Chapman, D., Thomlinson, W., Johnson, R. E., Washburn, D., Pisano, E., Gmur, N., Zhong, Z., Menk, R.,Arfelli F., and Sayers, D., 1997, Diffraction enhanced x-ray imaging, *Phys. Med. Biol*., **42**, 2015-2025.
5. Davis, T. J., Gao, D., Gureyev, T. E., Stevenson A. W., and Wilkins, S. W., 1995, Phase-contrast imaging of weakly absorbing materials using hard x-rays, *Nature*, **373**, 595-598.
6. Snigerev, A., Snigereva, I., Kohn, V., Kuznetsov, S., and Schelokov, I., 1995, On the possibilities of x-ray phase contrast microimaging by coherent high-energy synchrotron radiation, *Rev. Sci. Instrum*., **66**, 5486-5492.
7. Cloetens, P., Barrett, R., Baruchel, J., Guigay, J. P., and Schlenker, M., 1996, Phase objects in synchrotron radiation hard x-ray imaging, *J. Phys. D: Appl. Phys*., **29**, 133-146.
8. Born, M. and Wolrf, E., 1999, *Principles of Optics, 7th edition*, Cambridge University Press.
9. Margaritondo, G., and Tromba, G., 1999, Coherence-based edge diffraction sharpening of x-ray images: A simple model, *J. Appl. Phys*., **85**, 3406-3408.
10. Hwu, Y., Hsieh, H. H., Lu, M. J., Tsai, W. L., Lin, H. M., Goh, W. C., Lai, B., He, J. H., Kim, C. K., Noh, D. Y., Youn, H. S., Tromba, G., and Margaritondo, G., 1999, Coherence-enhanced synchrotron radiology: Refraction versus diffraction mechanisms, *J. Appl. Phys.*, **86**, 4613-4618.
11. Shastri, S.D., Mashayekhi, A., Fezzaa, K., Lee, W. K., Fernandez, P. B.,Tajiri, G. C., Ferguson, D. A., and Lee, P. L., "Bent Double-Laue Crystal Monochromator for High-Energy X-Rays", in APS Activity Report 1999, Argonne National Laboratory Report ANL-00/5 pp. 258--259. Also available via the APS website http://www.aps.anl.gov.
12. Bronnikov A.V., Theory of quantitative phase-contrast computed tomography, 2002, *J. Opt. Soc. Am. A*, **19** (3), 472-480.
13. Ginn, B. T. and Steinbock, O., 2003, Polymer surface modification using microwave-oven-generated plasma, *Langmuir*, **19**, 8117-8118.
14. Lucas, R., 1918, Uber das Zeitgesetz des kapillaren Aufstiegs von Flussigkeiten, *Kolloid Z*., **23**, 15-22.
15. Washburn, E. W., 1921, The Dynamics of Capillary Flow, *Phys. Rev*., **17**, 273-283.
16. Rideal, E. K., 1922, On the flow of liquids under capillary pressure, *Philos. Mag. Ser*., **6** (44), 1152.
17. Bosanquet, C. H., 1923, *Philos. Mag. Ser*. **6** (45), 525.
18. Marmur, A., 1992, in Modern Approach to Wettability: Theory and Applications (M.E. Schader and G. Loeb, Eds.), p. 327. Plenum, New York.
19. Ligenza, J. R., and Bernstein, R. B., 1951, The rate of rise of liquid in fine vertical capillaries, *J. Am. Chem. Soc*., **73**, 4636-4638.
20. Fisher, L. R., and Lark, P. D., 1979, Experimental study of the Washburn equation for liquid flow in very fine capillaries, *J. Colloid Interface Sci*., **69**, 486-492.
21. Malik, R. S., Laroussi, C. H., and de Becker, L. W., 1979, Experimental investigation of penetration. coefficient in capillary tubes, *Soil Sci*. **127**, 211-218.
22. Duarte, A. A., Strier, D. E., and Zanette, D. H., 1996, The rise of a liquid in a capillary tube revisited: A hydrodynamical approach, *Am. J. Phys*. **64**, 413-418.
23. Quéré, D., 1997, Inertial capillarity, *Europhys. Lett*., **39**, 533.
24. Quéré, D., Raphaël, E., and Ollitrault, J. Y., 1999, Rebounds in a capillary tube, *Langmuir*, **15**, 3679-3682.
25. Hamraoui, A., Thuresson, K., *et al*., 2000, Can a dynamic contact angle be understood in terms of a friction coefficient?, *J. Colloid Interface Sci*., **226**, 199-204.
26. Hamraoui, A., Thuresson, K., Nylander, T., Eskilson, K., and Yaminsky, V., 2000, Dynamic wetting and dewetting by aqueous solutions containing amphiphilic compounds, *Prog. Colloid Polymer Sci*., **116**, 113-119.
27. Christensen, F. E., Craig, W. W., Windt, D. L., Jimenez-Garate, M. A., Hailey, C. J., Harrison, F. A., Mao, P. H., Chakan, J. M., Ziegler, E., and Honkimaki, V., "Measured reflectance of graded multilayer mirrors designed for astronomical hard x-ray telescopes", 2000, *Nucl. Instrum. Meth*,. **A 451**, 572-581.

9. LIST OF SYMBOLS

n ..... refractive index
$1-\delta$..... real part of refractive index
β..... imaginary part of refractive index
k' ..... material wave vector
k ..... vacuum wave vector
λ..... wavelength, m
ρ..... density of material, g/cm^3
Z..... atomic number of material
Ψ_0..... amplitude of incident wave
Ψ_1..... amplitude of wave just after material
Ψ_P ..... amplitude of wave at measurement point
s_0 ..... sample to detector distance, m
R..... radon transform of a function

10. ASSISTANCE

For any question or problem concerning typing and organization of the paper please contact:

Dr. Alexandre Vabre
Phone +33 (0)1 69 08 50 47
Fax +33 (0)1 69 08 60 30
E-mail alexandre.vabre@cea.fr